Characterization of Time-Variant Wireless Channels in Railway Communication Scenarios

Stefan Zelenbaba[1], Lukas W. Mayer[2], Erislandy Mozo[3], Fabian Wirth[4], Reinhard Hladik[2], Arrate Alonso Gómez[3], Laura Bernadó[1], Martin Schiefer[2], Thomas Zemen[1]

[1]*Center for Digital Safety & Security*, *Austrian Institute of Technology GmbH*, Vienna, Austria, stefan.zelenbaba@ait.ac.at
[2]*CT REE ELM RFT-AT*, *Siemens AG Österreich*, Vienna, Austria
[3]*Electronics and Computer Science Dept.*, *Mondragon Unibertsitatea*, Arrasate-Mondragon, Spain
[4]*Havelländische Eisenbahn AG*, Elstal, Germany

***Abstract*—We present results from a train-to-infrastructure (T2I) and train-to-train (T2T) measurement campaign where we perform single-input-single-output channel sounding with a $150\,\mathrm{MHz}$ bandwidth, allowing us to resolve multi-path components with high precision. We analyze the measurements done for both T2I and T2T communication links, with trains going at speeds of maximum $20\,\mathrm{km/h} \approx 5.56\,\mathrm{m/s}$. Using low velocities allows us to run two trains behind each other on the same rail track with very short distances ($0 < \mathrm{d} < 200\,\mathrm{m}$). The analyzed data combined with GPS and video recordings serves for describing the geometry of the environment and developing a physical geometry-based stochastic channel model that enables virtual channel emulation for scenarios with trains moving at high velocities ($0 < \mathrm{v} < 300\,\mathrm{km/h} \approx 83.33\,\mathrm{m/s}$), but short distances. Characterizing the channel through empirically obtained data in such scenarios is still impossible in practice due to safety issues. Nevertheless, it presents a key step towards ultra-reliable low-latency link research for 5G use cases in the high-speed railway domain. We show that neighboring traffic and surrounding infrastructure has a big impact on the delay spread and that at extremely close distances, path loss variation depends on used antenna polarization.**

***Index Terms*—railway, 5G, wireless, URLLC, train-to-infrastructure, train-to-train**

I. Introduction

Ultra-reliable-low-latency (URLLC) links have the potential to revolutionize railways and are bound to play a key role in further train automation, launching the railways industry into the 5G era. Increasing reliability of communication links in critical areas such as level crossings, impacts the overall safety and security. For planning such communication systems, a thorough understanding of the underlying physical processes, namely wave propagation effects, is needed.

The measurement campaign performed in [1] investigates the influence of different infrastructure antenna heights for train-to-infrastructure (T2I) scenarios in rural environments. It presents the results in terms of path loss, Ricean K factor and root mean square (RMS) delay and Doppler spreads. However, the used bandwidth is $15\,\mathrm{MHz}$ which might not be sufficient in resolving multi-path components (MPC) in scatterer rich environments, with sufficient precision. A similar analysis is done in [2], where channel characteristics are observed for line-of-sight (LoS) T2I scenarios, at LTE carrier frequency of $2.6\,\mathrm{GHz}$ and with $10\,\mathrm{MHz}$ sounding bandwidth.

Apart from the communication with the infrastructure, the importance of train-to-train (T2T) communications is gaining on popularity in the high-speed railway (HSR) area, as it can truly benefit from low-latency links between trains. Due to large safety distances between trains (in the order of several km, depending on the train and train control systems), the tracks are strongly underutilized. Using URLLC for direct T2T communication allows the reduction of minimum safe distances, which is why it is so appealing to the industry.

So far, not much work has been done in the area of HSR T2T communications. The authors of [3] give a good overview of channel sounding parameters and compare the suitability of different channel model types for railway scenarios, highlighting the benefits of using geometry based stochastic channel models (GSCM). A GSCM presents a trade-off between the complexity of purely deterministic models and the flexibility of purely stochastic models. The need for such models in T2T communications is accented in [4] and a GSCM is proposed. However, the proposed model doesn't take into account obstructed LoS scenarios, additional rail traffic and extremely short distances. Another GSCM, for HSR T2I communication is proposed in [5].

In this paper we present the obtained data from our measurement campaign where we perform wide-band channel sounding and derive time-variant statistical parameters of the channel. The recorded videos and GPS coordinates of the node trajectories will be used to describe the environment and extrapolate a GSCM, to be used for emulating virtual wireless channels at much higher train speeds. To the best of our knowledge this is the first time a wireless channel modeling technique is considered for high-speed T2T communication links in order to explore train spacing smaller than the currently allowed minimum safety distance. Please note that wireless channels in such scenarios can not be measured in practice because of legal safety regulations.

Contributions of the Paper:

- We measure and characterize the channel for T2I and T2T scenarios, with trains moving at maximum speeds of $v_{\max} = 20\,\mathrm{km/h}$ with short distances ($0 < d < 200\,\mathrm{m}$)

- Based on the gathered data, we propose a methodology to develop a GSCM. This will allow us to emulate channels which would be impossible to measure, namely for high-speed ($200 - 300\,\mathrm{km/h}$) tailgating situations

II. Performance Indicators and Parameters

1) Characterization of rapidly time-varying channels: The channel transfer function $g(t, f)$, obtained on the receiver side (Rx) is sampled with the interval T_s, as

$$g[m, q] \coloneqq g(mT_\mathrm{S}, q/(NT_\mathrm{S}))\,, \tag{1}$$

with m being the discrete time index and $q \in \{1, ..., N\}$ the frequency (or subcarrier) index. Based on $g[m, q]$ we can estimate the local scattering function (LSF) [6]. The LSF [6] is a multi-taper estimate [7] of the scattering function, calculated for each stationarity region k sized $M \times N$. The discrete LSF is thus obtained as:

$$\hat{C}[k; n, p] = \frac{1}{IJ} \sum_{k}^{K} |\mathcal{H}^{(G_k)}[k; n, p]|^2\,. \tag{2}$$

The windowed time-variant frequency response $\mathcal{H}^{(G_k)}$ is defined as:

$$\mathcal{H}^{(G_k)}[k; n, p] = \sum_{m'=-M/2}^{M/2-1} \sum_{q'=-N/2}^{N/2-1} g[m' - m, q' - q] G_k[m', q'] e^{-j2\pi(pm' - nq')}\,, \tag{3}$$

where $n \in \{1, ..., N\}$ is the delay index and $p \in \{-M/2, ..., M/2 - 1\}$ the Doppler shift index. The window function $G_k[m', q'] = u_i[m' + M/2]\tilde{u}_j[q' + N/2]$ uses band-limited discrete prolate spheroidal sequences (DPSS) [8] u_i, indexed with $i \in \{1, ..., I\}$, and u_j, indexed with $j \in \{1, ..., J\}$, while $k = iJ + j$.

To describe the channel non-stationarity and the power dispersion in the delay-Doppler domain, we evaluate the time-variant power delay profile (PDP) and time-variant Doppler spectral density (DSD). The time-varying PDP and DSD can then be derived from the LSF as:

$$\hat{P}_\tau[k; n] = \frac{1}{M} \sum_{p=-M/2}^{M/2-1} \hat{C}[k; n, p]\,. \tag{4}$$

$$\hat{P}_\nu[k; p] = \frac{1}{N} \sum_{n=1}^{N} \hat{C}[k; n, p]\,. \tag{5}$$

A further simplification in describing the delay and Doppler spreads of the channel can be obtained with the root mean square (RMS) delay spread

$$\sigma_\tau[k] = \sqrt{\frac{\sum_{n=1}^{N} (n\tau_\mathrm{s})^2 \hat{P}_\tau[k; n]}{\sum_{n=1}^{N} \hat{P}_\tau[k; n]} - \bar{\tau}[k]^2}\,, \tag{6}$$

where

$$\bar{\tau}[k] = \frac{\sum_{n=1}^{N} (n\tau_\mathrm{s}) \hat{P}_\tau[k; n]}{\sum_{n=1}^{N} \hat{P}_\tau[k; n]}\,, \tag{7}$$

and τ_s is the delay domain resolution. The RMS Doppler spread is obtained as

$$\sigma_\nu[k] = \sqrt{\frac{\sum_{p=-M/2}^{M/2-1} (m\nu_\mathrm{s})^2 \hat{P}_\nu[k; p]}{\sum_{p=-M/2}^{M/2-1} \hat{P}_\nu[k; p]} - \bar{\nu}[k]^2}\,, \tag{8}$$

where

$$\bar{\nu}[k] = \frac{\sum_{p=-M/2}^{M/2-1} (m\nu_\mathrm{s}) \hat{P}_\nu[k; p]}{\sum_{p=-M/2}^{M/2-1} \hat{P}_\nu[k; p]}\,, \tag{9}$$

and ν_s is the Doppler domain resolution.

In order to eliminate spurious noise components and irrelevant MPCs from the calculations we use the power threshold criterion [9], with $35\,\mathrm{dB}$ from the peak value as the Rx sensitivity threshold, and $15\,\mathrm{dB}$ from the noise floor as the noise threshold.

The K factor presents the power ratio between the deterministic and the random component of the channel. We evaluate the K-factor using the method of moments (MoM) [10], for every 300 snapshots in time.

III. Equipment

1) Antennas: We perform single-input-single-output (SISO) channel sounding with with two types of antennas depending on the scenario. Directive antennas are mounted to radiate and receive vertical or horizontal polarization. They have $14\,\mathrm{dBi}$ gain each, while the omni-directional antennas have $4\,\mathrm{dBi}$ gain. The antenna arrangement is shown in Fig. 1.

The trajectory coordinates of both nodes are captured using two separate GPS receivers at each side. Videos of measurement runs are taken using a GoPro wide-angle camera mounted inside the Rx locomotive.

2) Sounder parameters and setup: The sounding measurements are conducted using the AIT channel sounder [11] which uses universal software radio peripheral (USRP) software defined radio (SDR) reconfigurable hardware.

The transmitter (TX) node of the sounder periodically sends out low crest factor sounding sequences. Each snapshot consists of the sounding sequence followed by a silent period. The sequence is formed from three copies of the sounding signal, with a total length of $12\,\mu\mathrm{s}$. The three signal copies include the cyclic prefix and a guard period (first half and the last half of a sounding signal copy, respectively), which leaves two signal copies that are used to obtain the over-sampled spectrum.

Fig. 1. Measurement equipment mounted on the end of each open freight wagon. Directive antennas (*a*) are mounted on a front facing plate, with one antenna having vertical (*V*), the other horizontal (*H*) polarization, and one spare. The omni-directional antenna (*b*) is mounted on a 2 m high pole.

A one pulse per second (1PPS) signal provided by a GPS disciplined rubidium oscillator, is used for synchronization. The oscillator also provides a 10 MHz frequency reference. The Rx records the receive signal with a sampling rate of $f_s = 160\,\mathrm{MHz}$. The channel transfer function $g[m, q]$ and the channel impulse response (CIR) $h[m, n]$ are derived from the recorded data in real-time, enabling live data evaluation.

A bandwidth of 150 MHz is used for the measurements, at a carrier frequency of 5.8 GHz. This frequency is chosen such that it complies with the ISM frequency band limits, and is still close to the 5.9 GHz band, used for planned vehicular applications in 5G. We use a transmit power of 21 dBm, while automatic gain control (AGC) is implemented on the receiver side. A certificate of exemption to use this transmit power, was obtained from the Bundesmetzagentur, which is the German radio frequency regulatory entity. The snapshot repetition rate is 500 μs, implying a maximum resolvable Doppler frequency shift of 1000 Hz at the chosen carrier frequency. This yields a maximum resolvable relative speed to be 186 km/h (51.67 m/s). The summary of the chosen channel sounding parameters is given in Tab. I.

TABLE I
CHANNEL SOUNDING PARAMETERS

Parameter	Value
Configuration	SISO
Carrier frequency	5.8 GHz
Measurement Bandwidth	150 MHz
Snapshot Interval	500 μs
Transmit Power	21 dBm

IV. CAMPAIGN SETUP

This measurement campaign presents the follow up to a previous one, described in [12]. The shunting yard in Elstal, Germany, is chosen as the measurement site due to its complex railways infrastructure and flexibility, i.e. the possibility to repeat measurement runs multiple times. Additionally, the facility allows for two trains to drive in the same track as well as enough curves and surrounding objects to recreate non-LoS (NLoS) situations (e.g. one train going behind a building). The site provides plenty of space with a rich scattering environment - other trains parked around neighboring tracks, overhead wiring, and live rail traffic in the vicinity.

The equipment is mounted on the end of open flat cargo wagons attached to locomotives, as depicted in Fig. 2 and 3.

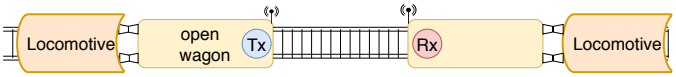

Fig. 2. Train composition diagram with both ends of the wireless link

Fig. 3. Photo of the fully mounted equipment on one side of the link. The node mounting with antennas is circled red

For calculations of the PDP and DSD, the stationarity region length of 120 ms ($M = 240$ snapshots) and the whole bandwidth of 150 MHz ($Q = 601$ frequency subcarriers) is used in evaluating the LSF. This provides a resolution of $\nu_s = 8.32\,\mathrm{Hz}$ and $\tau_s = 6.67\,\mathrm{ns}$ in the Doppler and the delay domain, respectively. The stationarity time of 120 ms is chosen in reference to the 40 ms derived in [13], due to the fact that the cars in [13] move at three times the speed of the trains we use.

Three distinctive scenarios are selected, to depict use cases of interest:

- **Scenario I** - T2I use case
- **Scenario II** - T2T use case - driving on the same track with variable distance
- **Scenario III** - T2T use case - parallel driving

Each of the scenarios is repeated multiple times in order to obtain meaningful statistics on the collected data, and better model evaluation. The results of a single run per scenario are chosen and presented in this paper.

1) Scenario I: We recreate the T2I communications use case. This is done by keeping one end of the link (in this case the mounted Tx antenna) static. The other train composition (Rx) is moving in direction either to or from the parked node, in a parallel track as shown in Fig. 4. The Tx is using an omni-directional antenna mounted on a pole at total height of $h \approx 3.5\,\mathrm{m}$ (see Fig. 1), while the Rx is equipped with the high-gain, directive antenna.

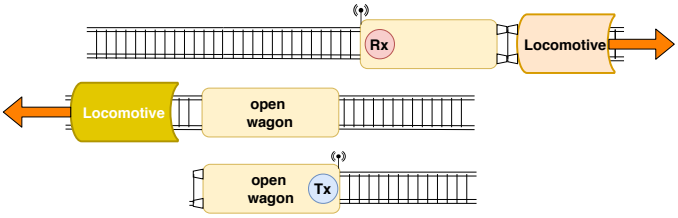

Fig. 4. Scenario I diagram of the chosen run. Another locomotive is detaching from a parked wagon and driving in the opposite direction from the Rx, thus causing additional MPCs to occur

2) Scenario II: The second scenario consists of three phases which are put together in one measurement run. It aims to recreate the coupling/uncoupling maneuver (introduced in [14]) in which two trains are driving behind each other with varying distance. This represents the main part of the smart train coupling use-case, where a train would drive behind another one and accelerate until it reaches a minimum safe distance (coupling). The two trains would then keep the distance constant by driving at the same speed (coupled mode), and when needed the train driving in the back would decrease speed and the distance between the two compositions would increase (uncoupling).

In our case this would require the trains to reach a certain velocity and distance before the maneuver could commence, thus using a large portion of the limited track length available at the site. For this reason we reverse the phase order in our measurements. Phase one simulates the uncoupling of two train compositions, where one train is driving away from the other. After that the trains drive behind each other, keeping the distance constant at $\mathrm{d} = 200\,\mathrm{m}$, resembling the coupled mode of two trains. In phase three, the front train decelerates while the other one approaches, to simulate coupling. Both nodes are using high-gain directive antennas.

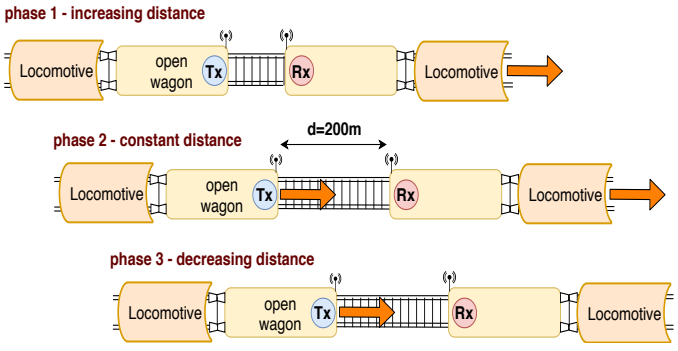

Fig. 5. Scenario II diagram showing three distinct phases. The arrows indicate train direction

3) Scenario III: In the third scenario, the trains are moving on parallel tracks, in opposite directions. This way the maximum relative speed of the nodes is doubled and with it the Doppler shifts. A train composition with roughly $4\,\mathrm{m}$ high metal freight wagons is placed on a track in between the two nodes to create NLoS conditions. There is a $\approx 2\,\mathrm{m}$ wide gap between each of the obstructing freight wagons.

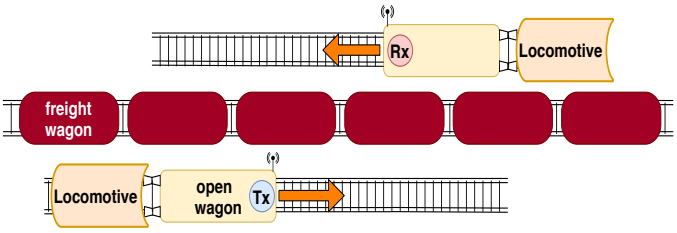

Fig. 6. Scenario III diagram with arrows depicting the directions of trains in a single run

V. Results

A. Scenario I

In the chosen measurement run, the Rx is moving away from the Tx antenna. In a parallel track between Tx and Rx there is another train going in the opposite direction as depicted on Fig. 4. The significant impact of this train on the RMS delay and Doppler spreads can be seen in Fig. 9, while the delay spread increases with environment complexity, and drops once the Rx train gets behind a building, thus obstructing the LoS.

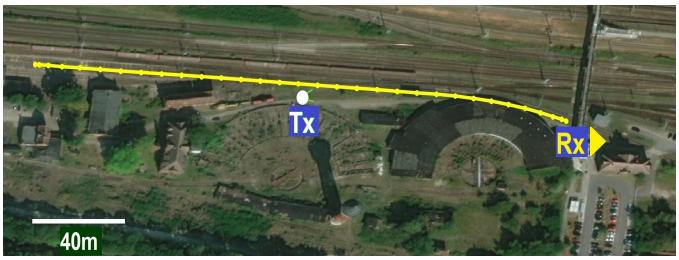

Fig. 7. Recorded GPS data of the Rx node trajectory and Tx node position (map source: World Imagery)

Fig. 8 shows the PDP and DSD of the chosen scenario run. The train driving in a parallel track and in the opposite direction from Rx introduces a strong MPC.

B. Scenario II

Due to the presence of bends in tracks, the trains can't maintain a constantly constant distance in phase 2. The PDP and DSD of recorded data are shown in Fig. 10. Both show distinct characteristics in all three phases. The components parallel to the LoS component (marked "1" and "3" on the figure) are a consequence of reflections between the carrying compositions, and they fade as the trains drive away from each other, but are always present. A richness in MPCs (marked "2" on the figure) is present due to the multitude of metallic objects such as parked train compositions and railway infrastructure.

The drop in signal power between $t \approx 160\mathrm{s}$ and $t \approx 190\mathrm{s}$ is a result of the leading locomotive going around a building, thus blocking a direct LoS path. The second path (marked as "4" in Fig. 10) at $t \approx 240\mathrm{s}$ appears when the leading train is passing between two parked train compositions, which apparently causes a strong path with higher delay. Closer inspection of PDP in phase one and beginning of phase two reveals two components parallel to LoS, corresponding to

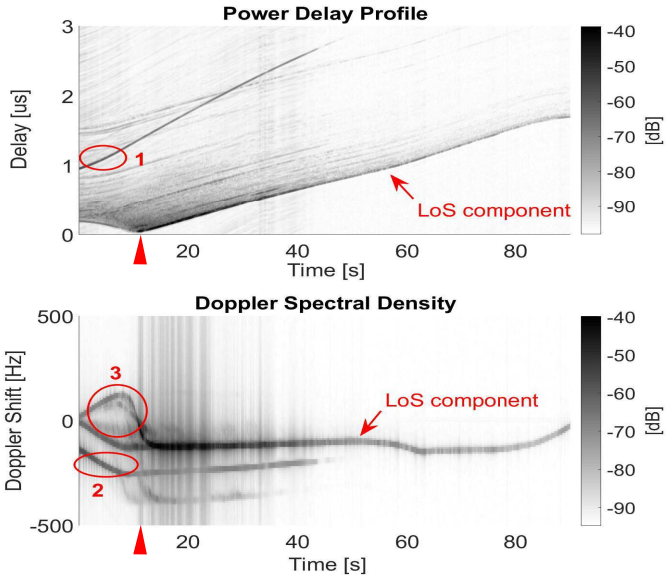

Fig. 8. Time variant PDP (top) and DSD (bottom) obtained for Scenario I. The point in time when nodes are passing each other is marked on the time axis with a triangle. The strong dark line having minimum delay and consequently shown at the bottom of the PDP is the LoS component of the received signal. Numbers "1" and "2" mark an MPC coming from the yellow train going in the opposite direction. The Doppler components coming from the reflections between the nodes themselves are marked with "3"

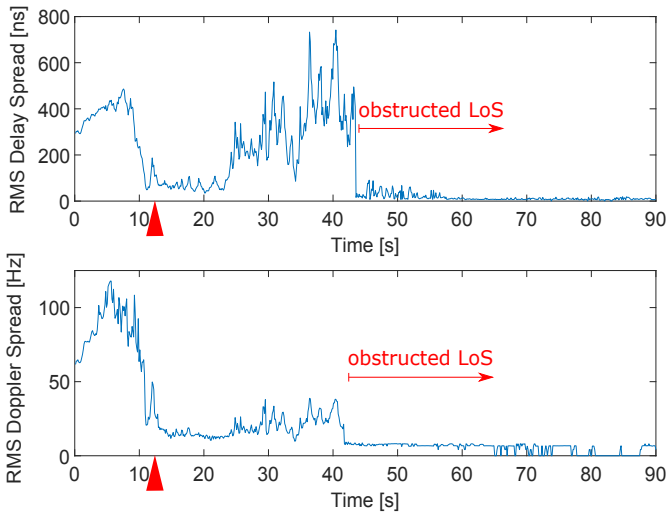

Fig. 9. RMS delay (top) and Doppler (bottom) spread obtained for Scenario I. The point in time when nodes are passing each other is marked on the time axis with a triangle.

reflection path distances of $\sim 12\,\mathrm{m}$ and $\sim 40\,\mathrm{m}$ longer than LoS. These originate from the train tracks, and at this point present another set of elevated, parallel tracks, approximately $10\,\mathrm{m}$ away from the trains.

In the very beginning of phase one and end of phase three, when trains are very close to each other, a periodic spike in path loss, RMS delay and Doppler could be distinguished, with RMS delay spread typically reaching $30\,\mathrm{ns}$.

Changing the antennae polarization to horizontal, has a significant effect on the variation of the signal. An increase of the

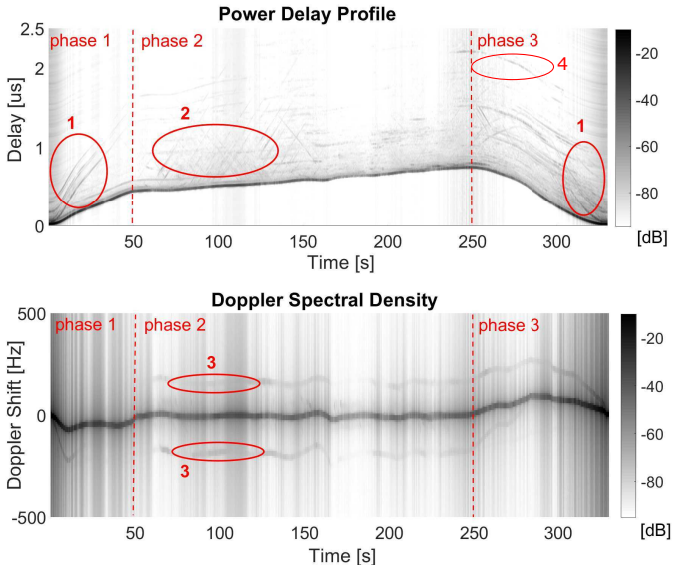

Fig. 10. Time variant PDP (top) and DSD (bottom) obtained for Scenario 2. The strong dark line having minimum delay and consequently shown at the bottom of the PDP depicts the LoS component. Number 1 and 3 mark reflections between the node carrying compositions in the PDP and DSD, respectively. 2 highlights an area rich with MPCs from surrounding objects

RMS delay spread by $20\,\mathrm{ns}$ has been observed. A comparison of the path loss of two polarization settings, when distance between the trains and velocity are decreasing is shown in Fig.11. The path loss variation versus distance is up to $10\,\mathrm{dB}$ stronger for horizontal polarization. The cause of this effect is the ground reflection that combines with the LoS component at the receiver. When using vertical polarization, the ground reflection is weaker because a significant part of the energy is directed into the ground and absorbed. The effect is strongest at the Brewster angle. At high distance between the trains (left region in Fig. 11), the variation versus distance is similar. This is because the reflection at the ground approaches very flat incident angles which cause high reflectivity regardless of the used polarization.

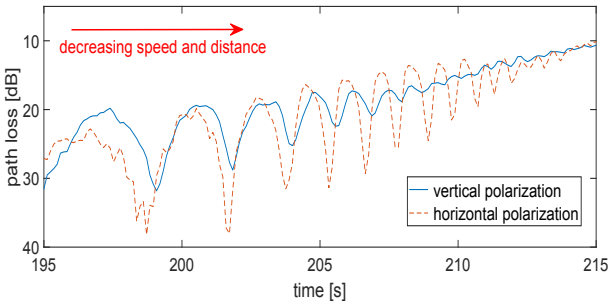

Fig. 11. Path loss comparison for vertically and horizontally polarized antennas. Speed and distance between the two trains are decreasing in the arrow direction (third phase of Scenario II).

C. Scenario III

Both train compositions are moving at the maximum speed of approximately $v = 20\,\mathrm{km/h}$, which means their maximum relative speed is doubled. The gaps between the freight

wagons cause periodical reflections, marked ”1” in Fig. 13. The vertical Doppler components marked ”1” in Fig. 13, are assumed to originate from reflections caused by gaps between the obstructing freight wagons. The components parallel to the LoS (marked ”2” and ”3” on the figure) are suspected to originate from the reflections between the locomotives but require further inspection.

Fig. 12. Recorded GPS data of the Tx and Rx nodes trajectories with marked directions (map source: World Imagery)

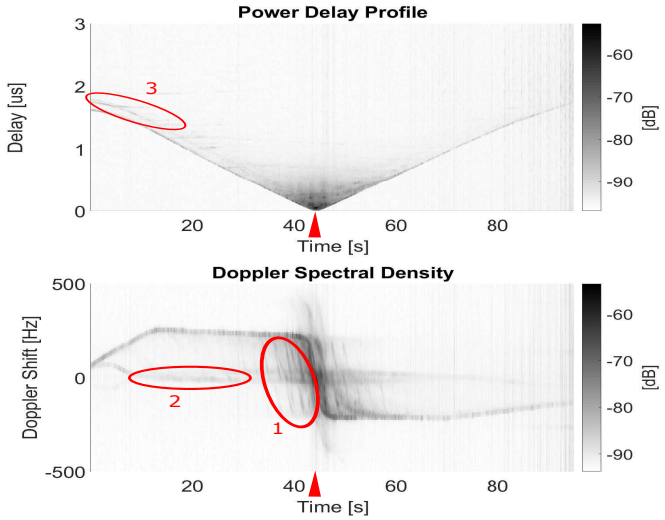

Fig. 13. Time variant PDP (top) and DSD (bottom) obtained for Scenario 3. The point in time when nodes are passing each other is marked on the time axis with a triangle. The reflections resulting from gaps between the obstructive freight composition are marked with ”1”. Numbers ”2” and ”3” mark the reflections made between the locomotives themselves.

VI. Conclusions and Further work

Based on the evaluated statistical data, we will develop a GSCM that can reproduce the same non-stationary fading process. Distinct objects such as buildings, rail tracks, other trains, masts and overhead wiring will be organized into geometrical clusters in order to make the model more flexible. A fast yet reliable algorithm for detecting and clustering MPCs is described in [15].

The obtained data provides a good base for further work and the proposed GSCM can be used for emulating channels in high-speed scenarios, thus substantially saving resources on work-intensive measurement campaigns. This will bring us one step closer to realizing smart-coupling train applications envisioned for 5G.

Acknowledgements

The measurement campaign described in the paper was done as a part of project SCOTT (www.scott-project.eu) that has received funding from the Electronic Component Systems for European Leadership (ECSEL) Joint Undertaking under grant agreement No 737422. This joint undertaking receives support from the European Unions Horizon 2020 research and innovation programme, and Austria, Spain, Finland, Ireland, Sweden, Germany, Poland, Portugal, Netherlands, Belgium, Norway.

The Havelländische Eisenbahn (HVLE) allowed access to their testing grounds for this campaign and provided vehicles, personnel and outstanding support in conducting the measurements.

References

[1] T. W. Tedesso, C. Rowe, C. R. Anderson, and C. B. Dietrich, “Propagation measurements at 5.8 ghz for railroad intelligent transportation systems,” in *2017 IEEE Wireless Communications and Networking Conference (WCNC)*, March 2017, pp. 1–6.

[2] T. Domínguez-Bolaño, J. Rodríguez-Piñeiro, J. García-Naya, and L. Castedo, “Experimental characterization of lte wireless links in high-speed trains,” *Wireless Communications and Mobile Computing*, vol. 2017, pp. 1–20, 09 2017.

[3] P. Unterhuber, S. Pfletschinger, S. Sand, M. Soliman, T. Jost, A. Arriola, I. Val, C. Cruces, J. moreno garcia loygorri, J. Pablo García-Nieto, C. Rodríguez, M. Berbineau, E. Echeverría, and I. Baz, “A survey of channel measurements and models for current and future railway communication systems,” *Mobile Information Systems*, vol. 2016, pp. 1–14, 06 2016.

[4] N. S. T. K. Paul Unterhuber, Michael Walter, “Joint delay and doppler frequency estimation for scatterer localization in railway environments,” in *13th European Conference on Antennas and Propagation (EuCAP 2019)*, 2019.

[5] L. Zhou, F. Luan, S. Zhou, A. F. Molisch, and F. Tufvesson, “Geometry-based stochastic channel model for high speed railway communications,” *IEEE Transactions on Vehicular Technology*, pp. 1–1, 2019.

[6] G. Matz, “On non-wssus wireless fading channels,” *IEEE Transactions on Wireless Communications*, vol. 4, no. 5, pp. 2465–2478, Sep. 2005.

[7] D. J. Thomson, “Spectrum estimation and harmonic analysis,” vol. 70, no. 9, pp. 1055 – 1096, September 1982.

[8] D. Slepian, “Prolate spheroidal wave functions, fourier analysis, and uncertainty — v: the discrete case,” *The Bell System Technical Journal*, vol. 57, no. 5, p. Slepian78, May 1978.

[9] N. Czink, “The random-cluster model – a stochastic mimo channel model for broadband wireless communication systemsof the 3rd generation and beyond,” Ph.D. dissertation, TU Wien, 2007.

[10] L. J. Greenstein, D. G. Michelson, and V. Erceg, “Moment-method estimation of the ricean k-factor,” *IEEE Communications Letters*, vol. 3, no. 6, pp. 175–176, June 1999.

[11] A. Albarracín, “Wireless wave propagation in city street canyons,” Master’s thesis, Lund University, Sweden, 2017.

[12] A. A. Gómez, E. Mozo, L. Bernadó, S. Zelenbaba, T. Zemen, F. Parrilla, and A. Alberdi, “Performance analysis of its-g5 for smart train composition coupling,” in *2018 16th International Conference on Intelligent Transportation Systems Telecommunications (ITST)*, Oct 2018, pp. 1–7.

[13] L. Bernadó, T. Zemen, F. Tufvesson, A. F. Molisch, and C. F. Mecklenbräuker, “The (in-) validity of the wssus assumption in vehicular radio channels,” in *2012 IEEE 23rd International Symposium on Personal, Indoor and Mobile Radio Communications - (PIMRC)*, Sep. 2012, pp. 1757–1762.

[14] U. Bock and G. Bikker, “Design and development of a future freight train concept – “virtually coupled train formations”,” *IFAC Proceedings Volumes*, vol. 33, no. 9, pp. 395 – 400, 2000, 9th IFAC Symposium on Control in Transportation Systems 2000, Braunschweig, Germany, 13-15 June 2000.

[15] F. Luan, A. F. Molisch, L. Xiao, F. Tufvesson, and S. Zhou, “Geometrical cluster-based scatterer detection method with the movement of mobile terminal,” in *2015 IEEE 81st Vehicular Technology Conference (VTC Spring)*, May 2015, pp. 1–6.